An experimental and constitutive modeling study on the large strain deformation and fracture behavior of PC/ABS blends

J. Hund, J. Naumann, Th. Seelig[1]

Institute of Mechanics, Karlsruhe Institute of Technology, Kaiserstrasse 12, 76131 Karlsruhe, Germany

Abstract

Two rubber-toughened thermoplastic polymer blends with different volume fractions of polycarbonate (PC) and acrylonitrile-butadiene-styrene (ABS) are analyzed experimentally as well as by constitutive models and finite element simulations with regard to their large strain deformation and fracture behavior. Special emphasis thereby is devoted to the overall plastically dilatant behavior of these materials which results from microscale damage mechanisms. Not considering the latter in detail, it is shown that several material models of different complexity may well capture the macroscopic true stress-strain response and the plastic dilatancy of PC/ABS blends under uniaxial loading. The suitability of these models to describe the behavior of the blends under more complex loading conditions, however, turns out to be ambivalent and depends on the material composition, i.e. the PC vs. ABS content. This issue is analyzed by means of finite element simulations of fracture tests where numerical predictions in terms of the overall force-displacement response and the local evolution of the crack-tip plastic zone are compared with experimenral findings.

Keywords

Rubber-toughened polymers, PC/ABS blends, constitutive modeling, plastic dilatancy, fracture simulation

[1]Corresponding author: Tel.: +49-721-608-43714; Fax.: +49-721-608-47990, Email: thomas.seelig@kit.edu

1 Introduction

PC/ABS blends, i.e. mixtures of the glassy thermoplastic polycarbonate (PC) and acrylonitrile-butadiene-styrene (ABS) are used in many technical applications, for instance, because of their ductility as well as enhanced fracture toughness. Since the ABS phase is itself a mixture of the glassy thermoplastic styrene-acrylonitrile (SAN) and finely dispersed rubber (butadiene) particles, PC/ABS is referred to as a ternary blend. From a mechanics point of view, commercial grades differ essentially by their composition (e.g. amount of PC, amount of rubber in ABS) and – consequently – their mechanical properties, e.g. [3, 8, 15, 16, 17, 21, 22, 28, 29, 32]. Further influences on the latter are ascribed to the molecular weight of the individual constituents and the processing induced blend morphology.

Owing to their practical importance, PC/ABS blends have been analyzed in many experimental studies (see above), yet theoretical investigations concerning the constitutive modeling of their mechanical behavior so far are rare. For instance, the large strain rate-dependent behavior under uniaxial tension has been fitted by a phenomenological 1D model in [7], and the (plastically incompressible) response under compressive loading was described by a rate-dependent J_2-plasticity model in [31]. The dilative behavior under tensile loading is very seldomly reported, e.g. [14], and so far not adequately considered in constitutive modeling. Qualitative micromechanical studies concerning the influence of the blend composition on the macroscopic response were carried out in [25, 26], yet without relating these effects quantitatively to the true (experimental) behavior. In fact, multiscale approaches of this kind typically suffer from a lack of reliable data about the constituent behavior within the composite. For practical applications, e.g. involving structural finite element (FE) analyses, however, efficient macroscopic models are needed which quantitatively capture the material behavior under complex loading states up to failure.

In the present work, two commercial PC/ABS grades with different composition in terms of PC and ABS content are analyzed experimentally regarding their large strain response under uniaxial tension as well as fracture conditions. Of particular importance thereby is the macroscopic plastic dilatancy which is known to originate from various micromechanisms such as rubber particle cavitation, plastic void growth and crazing (occuring in the ABS phase) as well as debonding along the interface between PC and ABS, e.g. [2, 8, 15, 16, 17]. The focus of the present work, however, is merely on the overall effect of these mechanisms. Their contribution to the macroscopic behaviour of PC/ABS depends on the different PC and ABS contents in the blend material, with overall dilation originating mainly from the ABS phase. In order to identify and analyze an appropriate macroscopic description of PC/ABS blends, three material models of different structure – all accounting for plastic dilatancy – are compared with regard to their capability to capture the experimentally observed behavior. These models are the classical *Drucker-Prager* model, e.g. [6], and the *Raghava* model, e.g. [23, 24], which differ by the shape of the yield surface, as well as a *Green/Gurson*-like model [9, 12] which in contrast to the aforementioned two accounts for an evolution of porosity with plastic flow. The models, when calibrated to the uniaxial tensile response (often solely available for material parameter identification) all prove to well capture the rate-dependent true stress-strain behavior including the evolution of volumetric strain of the two tested PC/ABS materials over large strains. Once this agreement given, the questions of primary interest in this work is in how far either of these models is suited to describe the experimentally observed behavior in case of more complex loading situations such as notched specimens and crack propagation, i.e. at higher stress triaxialities which are typically not as often considered in the calibration of constitutive models. The present work thus appears to be a first systematic study towards the constitutive modeling and a sound calibration of the large strain (visco)-plastically dilatant behavior of PC/ABS blends.

The paper is organized as follows: In Sect. 2 the experimental study is described where digital image correlation (DIC) is used to analyze the local strain distribution in unnotched and notched specimens. This allows to determine the true stress-strain response as well as the evolution of volume strain under uniaxial tension. Section 3 is devoted to the presentation of the constitutive models, while their calibration to the experimental data is specified in Sect. 4. In Sect. 5 the different material models are employed in 3D finite element studies of the fracture behavior of the two PC/ABS blends in case of single-edge-notch-tension (SENT) specimens. Numerical results are compared to experimental findings and are analyzed with regard to the crack-tip plastic zone as well as the overall force-displacement response during specimen failure. A summary of this study and conclusions are provided in Sect. 6.

Throughout the paper, symbolic notation of tensors is used, with second order tensors written in bold face $\boldsymbol{A}$ and fourth order tensors as $\mathbb{A}$. The symbol ":" thereby means a double contraction (e.g. scalar product of second order tensors) and "$\otimes$" denotes the dyadic product.

2 Experimental study

The experimental study in this work comprises monotonic uniaxial tensile tests with large strains up to failure as well as fracture tests on single-edge-notch-tension (SENT) specimens. Two commercial PC/ABS blends Bayblend™ T45 and Bayblend™ T85 by Covestro are examined. Bayblend™ T45 features a PC content of about 45 % whereas the amount of PC in Bayblend™ T85 is about 70 % [27]. For clarity, Bayblend™ T45 is in the following referred to as PC/ABS(45/55) and Bayblend™ T85 as PC/ABS(70/30), respectively. The experiments were carried out on a servo-hydraulic testing machine (Instron) at room temperature. Every test was performed with at least three replicates for averaging purposes. Mechanical clamps were used to attach the specimens to the testing machine. The strain field on the plane specimen surface was determined via 2D digital image correlation (DIC, Limess Q-400-2D [20]) with a camera resolution of 2 MPixel and a maximum frame rate of $20\,\mathrm{sec}^{-1}$.

2.1 Uniaxial tensile tests

The uniaxial tensile tests on specimens as sketched in Fig. 1 were performed at two different values of the nominal strain rate, $\dot{\varepsilon} = 0.01\,\mathrm{sec}^{-1}$ and $\dot{\varepsilon} = 0.1\,\mathrm{sec}^{-1}$, defined as the rate of overall specimen elongation divided by the gauge length of 12 mm. Since only

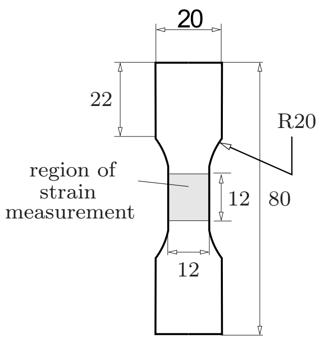

Figure 1: Geometry of plane tensile test specimen in mm (thickness 3 mm).

the strain field on the plane specimen surface was measured (Fig. 2), the assumption of equal through-thickness and in-plane transverse strains ε_{tr} was made. The true (Cauchy) stress σ hence was determined from the applied force F and the initial (undeformed) cross section A_0 according to

$$\sigma = \frac{F}{A_0 \exp(2\varepsilon_{tr})} \tag{1}$$

where ε_{tr} is the logarithmic transverse strain.

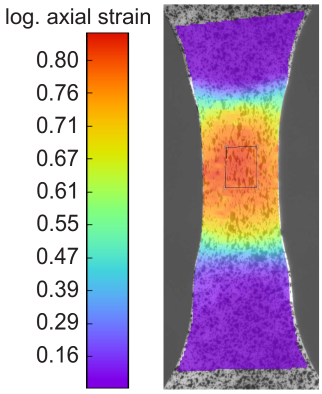

Figure 2: Contours of logarithmic axial strain in PC/ABS(45/55) specimen obtained from DIC.

Figure 3 shows the thus determined true stress-strain response of the two PC/ABS materials which both feature a small (approximately linear) elastic range and a distinct yield point, followed by softening and progressive rehardening up to failure – as typical for ductile amorphous thermoplastics. Owing to its higher PC content, PC/ABS(70/30) exhibits a significantly (almost 20%) higher stress level in the plastic strain regime than PC/ABS(45/55). This corresponds to other experimental findings reported in the literature, e.g. [3, 22, 28, 29]. The progressive rehardening at large strains is somewhat more pronounced in case of PC/ABS(70/30) which may also be ascribed to its higher PC content. The individual test data in Fig. 3 indicate a rather small amount of scatter in the stress level but a significant scatter in the failure strain with values between 0.6 and 0.8 for both materials.

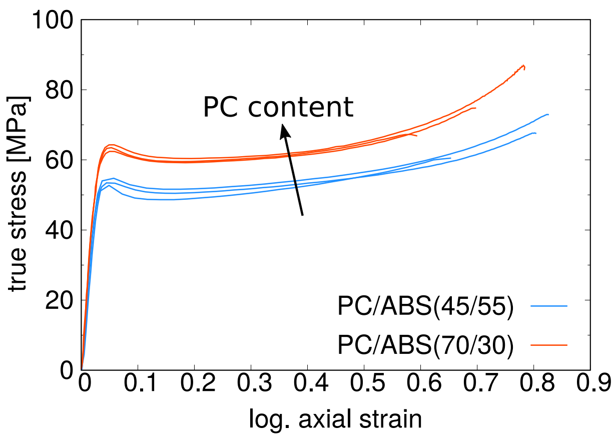

Figure 3: Composition dependent true stress-strain behavior of PC/ABS at a strain rate of $\dot{\varepsilon} = 0.1\,\mathrm{sec}^{-1}$.

As shown in Fig. 4, both PC/ABS blends exhibit a pronounced plastic dilatancy under uniaxial tension. This volume strain can be ascribed to microscale deformation and damage mechanisms such as rubber cavitation, void growth and crazing in the ABS phase, e.g. [2, 8, 17], as well as eventual interface debonding [15]. The somewhat larger dilation of PC/ABS(45/55) can be attributed to its higher ABS content. For strains larger than about 0.6, the difference in the dilatancy of the two materials becomes significant. The volume strain then decreases again with axial strain, particularly for PC/ABS(70/30). This transition may heuristically be explained as follows: PC deforms essentially by isochoric shear yielding, whereas ABS is known to display itself a pronounced dilatancy due to above mentioned mechanisms. In the early stage of plastic straining with an almost constant (plateau-like) stress response of both PC/ABS blends (Fig. 3) this leads to only a gradually larger dilation of the ABS-rich material. At larger strain (> 0.6), however, where PC hardens much stronger than ABS (e.g. [11],[13]) the overall load is increasingly borne by the (incompressible) PC phase which thus dominates the overall response of PC/ABS. In the range of progressive hardening this leads to a decrease of volume strain with axial strain with a stronger effect in case of the PC-rich material (Fig. 4).

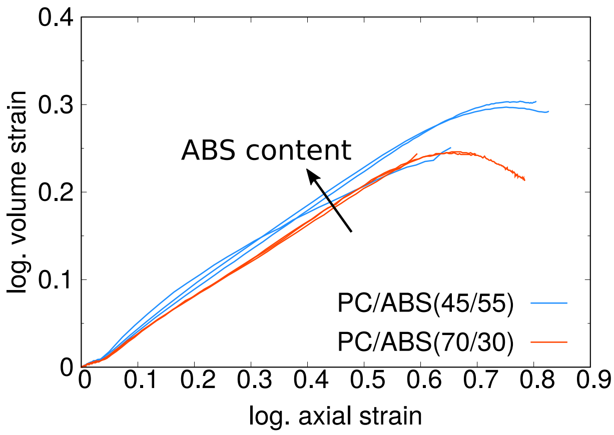

Figure 4: Composition dependent dilation behavior of PC/ABS at a strain rate of $\dot{\varepsilon} = 0.1\,\mathrm{sec}^{-1}$.

As typical for thermoplastic polymers, PC/ABS blends exhibit a rate-dependent behavior with a higher stress level for higher strain rates. However, since the rate-dependence of PC/ABS is not in the scope of the present study, corresponding experimental results are for brevity only shown in Sect. 4 in conjunction with the calibration of constitutive models.

2.2 Fracture tests

Fracture tests were carried out on single-edge-notch-tension (SENT) specimens (Fig. 5) with a cross head speed of 1 mm/sec. The notch radius in these tests was 1 mm while the specimen thickness was 3 mm.

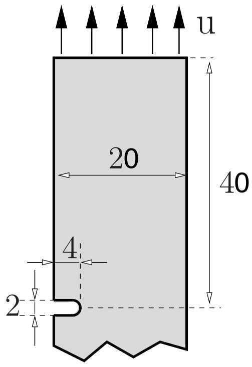

Figure 5: SENT specimen geometry (in mm, thickness 3 mm) used in fracture tests.

The distribution of the strain in the tensile direction obtained from digital image correlation (DIC) at the specimen surface is shown in Fig. 6 for both materials at two successive loading stages (overall specimen elongation u). As characteristic for rubber-toughened

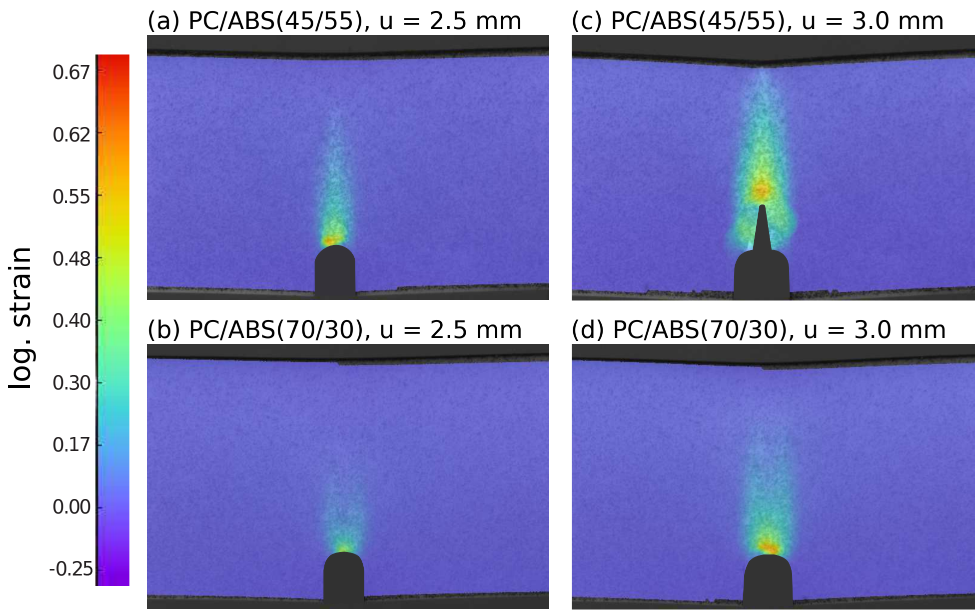

Figure 6: Contours of log. strain in tensile direction (horizontal) obtained from DIC showing plastic zone formation at notch in SENT specimen for PC/ABS(45/55) and PC/ABS(70/30) at two different values of overall specimen elongation u.

polymers, an elongated zone of intense deformation develops ahead of the notch; this in fact represents the plastic deformation zone since strains there are much larger than the elastic strains (cf. Fig. 3). Owing to the lower yield strength of PC/ABS(45/55) the plastic zone in this material (Fig. 6a and c, top) is somewhat larger than that in PC/ABS(70/30) shown in Fig. 6b and d (bottom). An interesting observation is that the plastic zone in the PC-rich material PC/ABS(70/30) splits up into two branches at some distance ahead of the notch (Fig. 6b and d) which might be indicative of a through-thickness slip mechanism. In the ABS-rich material PC/ABS(45/55) this effect is not visible (Fig. 6a and c).

The recorded force displacement curves (Fig. 7) show a higher peak load and a slightly larger overall displacement at complete specimen failure in case of PC/ABS(70/30). The earlier onset of crack propagation in PC/ABS(45/55) seen in Fig. 6c at a specimen elongation of 3 mm is also reflected in the force displacement behavior (Fig. 7) where at this loading stage the curve of PC/ABS(45/55) is already declining whereas the curve of PC/ABS(70/30) has not yet reached its peak value.

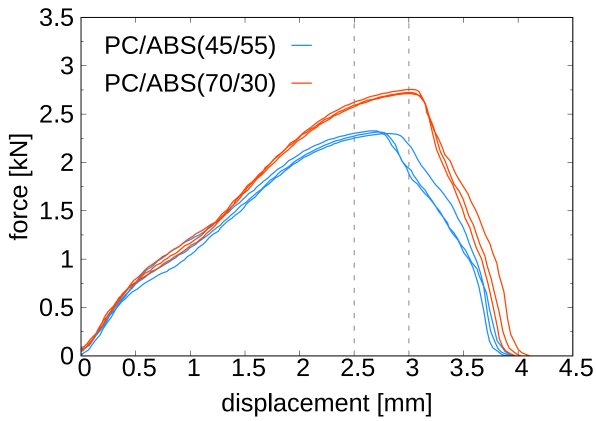

Figure 7: Force displacement curves of SENT specimen for both materials. Dashed vertical lines correspond to snap-shots in Fig. 6.

3 Constitutive modeling

3.1 Elastic-viscoplastic behavior - general structure

In the following, the general structure of the constitutive models employed in this work is presented. In accordance with the experimental findings (Fig. 3), it accounts for small elastic and large viscoplastic strains. Formulating the constitutive equations in rate form is convenient in view of the subsequent numerical implementation. The total rate-of-deformation tensor is hence additively split into its elastic and viscoplastic part as $\boldsymbol{D} = \boldsymbol{D}^e + \boldsymbol{D}^p$. The elastic part enters the hypo-elastic relation

$$\overset{\triangledown}{\boldsymbol{\sigma}} = \mathbb{C} : (\boldsymbol{D} - \boldsymbol{D}^p) \tag{2}$$

where $\overset{\triangledown}{\boldsymbol{\sigma}}$ denotes the Jaumann rate of the Cauchy stress tensor $\boldsymbol{\sigma}$ and $\mathbb{C}$ is the isotropic fourth order elasticity tensor

$$\mathbb{C} = \frac{E}{1+\nu}\left(\mathbb{I} + \frac{\nu}{1+2\nu}\boldsymbol{I}\otimes\boldsymbol{I}\right) \tag{3}$$

with Young's modulus E, Poisson's ratio ν and the fourth and second order identity tensors $\mathbb{I}$ and $\boldsymbol{I}$, respectively. The inelastic part of the rate-of-deformation tensor is taken to be governed by the normality flow rule

$$\boldsymbol{D}^p = \dot{\varepsilon}^p \boldsymbol{N} \qquad \text{with} \qquad \boldsymbol{N} = \frac{\partial\Phi/\partial\boldsymbol{\sigma}}{\sqrt{\dfrac{\partial\Phi}{\partial\boldsymbol{\sigma}} : \dfrac{\partial\Phi}{\partial\boldsymbol{\sigma}}}} \tag{4}$$

determined from an isotropic yield function of the general structure

$$\Phi(\boldsymbol{\sigma}, \varepsilon^p) \equiv \tilde{\Phi}(\sigma_e, \sigma_m) - k(\varepsilon^p) \quad . \tag{5}$$

The latter is taken to depend on the equivalent von Mises stress $\sigma_e = \sqrt{\frac{3}{2}\boldsymbol{\sigma}' : \boldsymbol{\sigma}'}$ and the hydrostatic stress $\sigma_m = \frac{1}{3}\boldsymbol{\sigma} : \boldsymbol{I}$, where $\boldsymbol{\sigma}'$ denotes the deviatoric part of the stress tensor. Through the dependence of the yield function on the hydrostatic stress in conjunction with the associated flow rule (4), the model features plastic dilatancy as necessary to appropriately represent the behavior of PC/ABS blends shown in Fig. 4. Despite the well known fact that thermoplastic polymers exhibit a pronounced kinematic hardening (Bauschinger effect) due to molecular alignment, e.g. [4, 30], yet in view of the essentially monotonic loading situations considered in the present work, hardening (as well as intrinsic softening, Fig. 3) is here simply modeled in an isotropic fashion through the evolution of the yield strength $k(\varepsilon^p)$ in (5) with the accumulated plastic strain $\varepsilon^p = \int_0^t \sqrt{\boldsymbol{D}^p : \boldsymbol{D}^p}\, dt$. This dependence is approximated by the relation

$$k(\varepsilon^p) = \beta_1 + \beta_2 \exp(-\beta_3 \varepsilon^p) + \beta_4 (\varepsilon^p)^{\beta_5} \tag{6}$$

with material parameters β_1 to β_5, which features exponential softening at small plastic strains and subsequent power-law rehardening. It should be mentioned that a much more sophisticated model for rubber-toughened (porous) glassy polymers accounting, e.g., for kinematic hardening has been developed in [4].

Rate-dependence is described by an Eyring-type relation for the inelastic strain rate

$$\dot{\varepsilon}^p = \dot{\varepsilon}_0 \exp\left(A\,\Phi\right) \tag{7}$$

with a reference strain rate $\dot{\varepsilon}_0$ and a further material parameter A. The latter might be taken to depend on temperature which, however, is not an issue here.

3.2 Yield functions

Three different well established isotropic yield functions accounting for a dependence on hydrostatic stress σ_m – which in conjunction with the assumed associated flow rule give rise to plastic volume strain – are considered here to describe the inelastic behavior of the PC/ABS blends:

Drucker-Prager [6] $$\Phi_{\mathrm{DP}} \equiv \sigma_e + \alpha_{\mathrm{DP}}\,\sigma_m - k_{\mathrm{DP}}(\varepsilon^p) \quad , \tag{8}$$

Raghava [23, 24] $$\Phi_{\mathrm{R}} \equiv \sqrt{\sigma_e^2 + \alpha_{\mathrm{R}}\,\sigma_m} - k_{\mathrm{R}}(\varepsilon^p) \quad , \tag{9}$$

Green/Gurson-like [9, 12] $$\Phi_{\mathrm{G}} \equiv \frac{1}{1-f}\sqrt{\sigma_e^2 + \alpha_{\mathrm{G}} f \sigma_m^2} - k_{\mathrm{G}}(\varepsilon^p) \quad . \tag{10}$$

The material parameter α individually controls the dependence of the yield functions on hydrostatic stress. The interrelation between the von Mises and the hydrostatic stress is linear in case of the Drucker-Prager (DP) model while it is parabolic in the Raghava (R) model. Following Green [9] or simplifying slightly the Gurson model [12], a quadratic dependence on both σ_e and σ_m is considered in the third yield function (G). In addition, the latter explicitly depends on the porosity f which according the conservation of mass is taken to evolve as $\dot{f} = (1-f)\,\mathrm{tr}(\boldsymbol{D}^p)$. Hence, the Drucker-Prager and the Raghava model differ only by the (fixed) shape of the "yield surface", the size of which varies with $k(\varepsilon^p)$, whereas in case of the Green/Gurson-like model both the shape and size of the "yield surface" change with the evolving porosity.

Figures 8 and 9 show the initial yield loci calibrated to the experimental data for PC/ABS(45/55) and PC/ABS(70/30) under uniaxial tension, i.e. at a stress triaxiality of $\eta := \sigma_m/\sigma_e = 1/3$. The fact that the different yield surfaces are not perfectly tangential for uniaxial tension is attributed to fitting the evolution of volume strain (see Figs. 11 and 12 below) as good as possible not only at the onset of yield but over the entire range of axial strains up to failure. The different slopes of the initial yield surfaces in Figs. 8 and 9 for uniaxial tension ($\eta = 1/3$) correspond to the different slopes of the curves in Figs. 11 and 12 at the onset of yield, i.e. at an axial strain of approximately 0.05. Also indicated as straight diagonal lines in Figs. 8 and 9 are elevated stress triaxialities of $\eta = 1$ and $\eta = 3$ as encountered in simulations of notched tensile specimens below (Sect. 5).

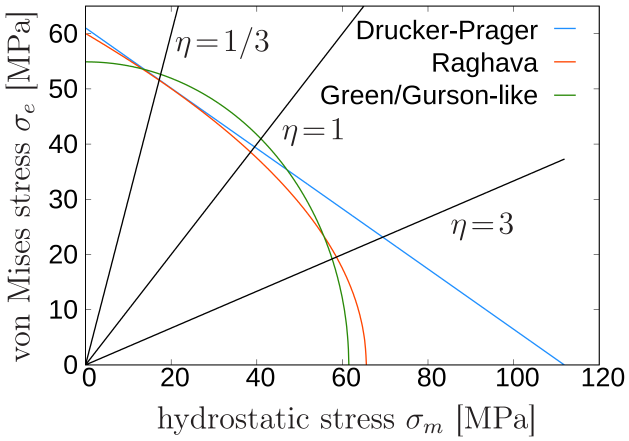

Figure 8: Initial yield loci in σ_m-σ_e-plane calibrated for PC/ABS(45/55) under uniaxial tension ($\eta = 1/3$).

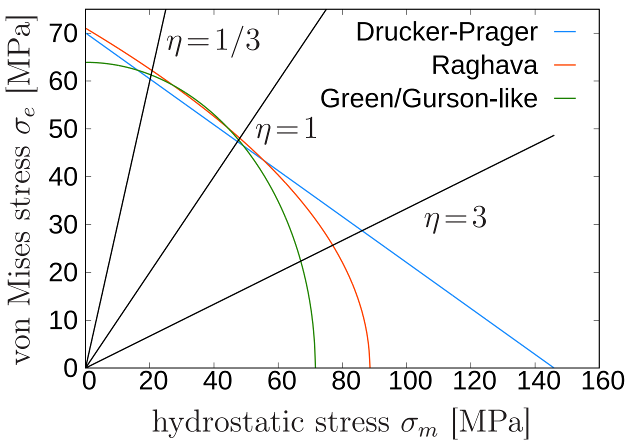

Figure 9: Initial yield loci in σ_e-σ_m-plane calibrated for PC/ABS(70/30) under uniaxial tension ($\eta = 1/3$).

4 Parameter calibration

The different constitutive models considered here are chosen as simple as possible (e.g. each with a constant value of the parameter α in the yield functions (8), (9) and (10)). They are calibrated for both materials to match the experimental data of the uniaxial tensile tests in terms of the true stress-strain response (Fig. 10) as well as the evolution of volume strain (Figs. 11 and 12) as good as possible over a large range of deformation, i.e. up to failure at a logarithmic strain of about 0.8. Figure 10 shows that the uniaxial stress-strain response of both materials is captured quite well by all three models with individual parameter values listed in the Appendix.

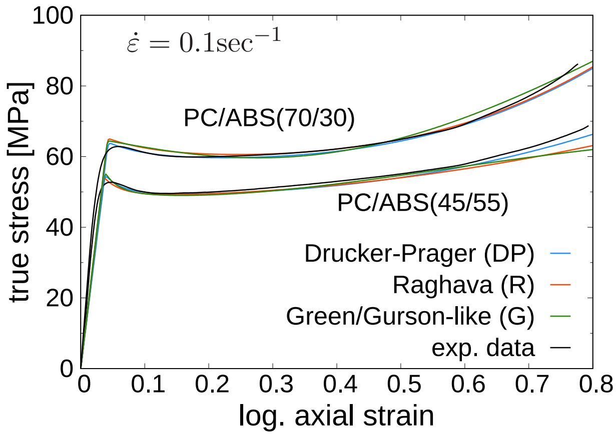

Figure 10: Uniaxial stress-strain responses of all models compared to experimental data for PC/ABS(45/55) and PC/ABS(70/30) at a strain rate of $\dot{\varepsilon} = 0.1$ sec^{-1}.

Also reasonably well captured is the accompanying evolution of volume strain (Figs. 11 and 12). Only the saturation or even decrease of volume strain between an axial strain of 0.6 and 0.8 is not accounted for in the constitutive models.

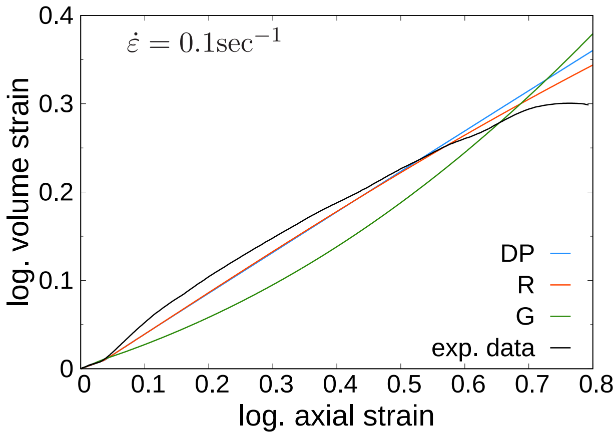

Figure 11: Dilation behavior of all models under uniaxial tension compared to experimental data for PC/ABS(45/55).

Finally, the experimental data for two different strain rates allowed to calibrate the rate-dependence of the material models in terms of the parameters $\dot{\varepsilon}_0$ and A in (7) as shown exemplarily for PC/ABS(45/55) in Fig. 13. The complete sets of parameters for each model is given in Tables 1 and 2 in the Appendix.

As the three different material models have all proven to reasonably well capture the mechanical behavior of PC/ABS blends under uniaxial tension, it is instructive to look at their performance under higher stress triaxialities. Figures 14 and 15 therefore depict the true stress-strain and volumetric strain response of the Drucker-Prager, Raghava and

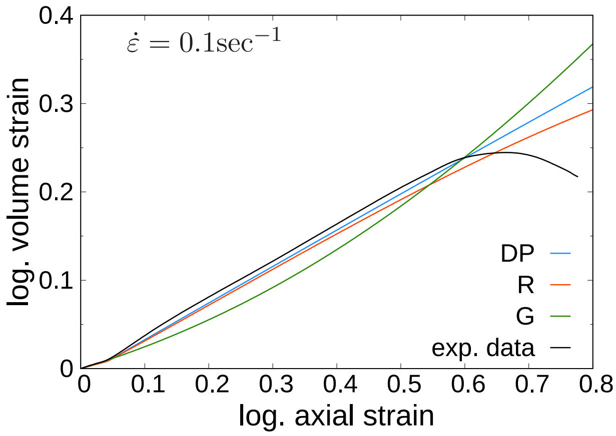

Figure 12: Dilation behavior of all models under uniaxial tension compared to experimental data for PC/ABS(70/30).

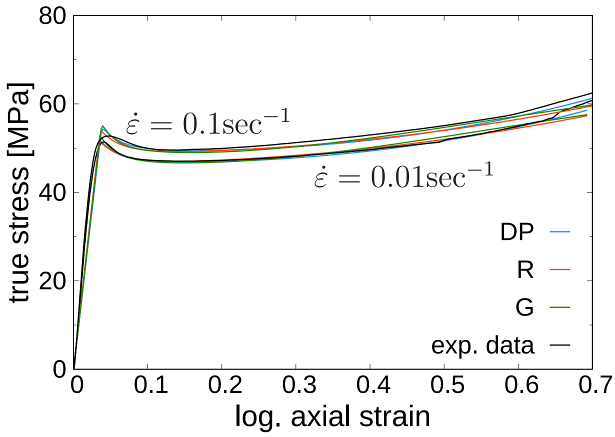

Figure 13: Uniaxial stress-strain responses of all models compared to experimental data for PC/ABS(45/55) at two different strain rates.

Green/Gurson-like model subjected to tension with a stress triaxiality of $\eta = \sigma_m/\sigma_e = 1$ and $\eta = 3$, respectively. For $\eta = 1$ the Drucker-Prager and the Raghava model yield almost identical results since at this stress triaxility the shape (normal direction) of their "yield surfaces" is quite similar (see Figs. 8 and 9). Significant differences in terms of a reduced stress level (Fig. 14) and an increased volume strain (Fig. 15) predicted by the Raghava model in comparison with the Drucker-Prager model only show up at the higher stress triaxility of $\eta = 3$ where the yield loci clearly depart (Figs. 8 and 9). Both the Drucker-Prager and the Raghava model feature a progressive hardening response (Fig. 14) even at elevated stress triaxilities. In contrast, the Green/Gurson-like model, which is governed by the evolving porosity that increases with plastic volume strain and thus causes a shrinkage of the "yield surface", exhibits a softening stress-strain response for both elevated stress

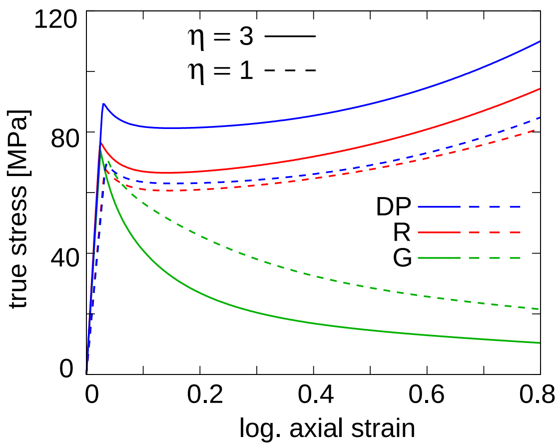

Figure 14: Tensile true stress-strain response of the Drucker-Prager, the Raghava and the Green/Gurson-like model under elevated stress triaxialities η.

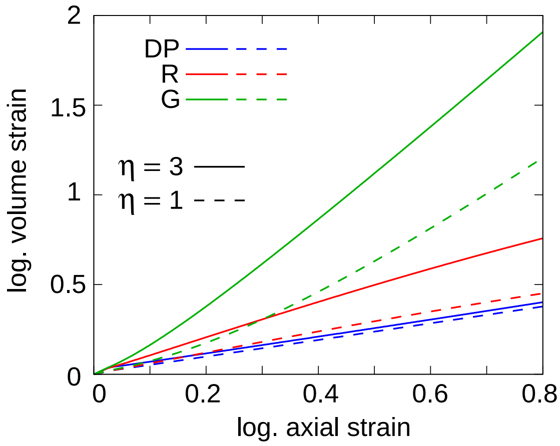

Figure 15: Evolution of volume strain with axial strain predicted by the three models under elevated stress triaxialities η.

triaxialities (Fig. 14). That means that in case of the Green/Gurson-like model the plastic volume strain (increasing porosity) counteracts and, in fact, dominates strain hardening exhibited (Fig. 10) under uniaxial tension ($\eta = 1/3$). The effect of the different models' response at elevated stress triaxialities emerges in the following numerical simulations of plastic zones in notched tensile specimens.

5 Numerical studies

Though available, more or less, in commercial finite element codes, the material models considered here have for consistency all been implemented as user material routines in the finite element (FE) package Abaqus/Explicit [5]. Thereby, an efficient semi-implicit time integration of the constitutive equations is employed where only the scalar quantity ε^p is updated implicitly whereas the tensorial direction $\boldsymbol{N}$ of plastic flow (see (4)) is updated in an explicit manner, as suggested e.g. in [1].

FE simulations of the SENT tests presented in Sect. 2.2 are carried out in order to analyze the performance of the different material models in complex loading situations. Employing symmetry with respect to the center plane, only half of the SENT specimen was modeled and corresponding boundary conditions of zero normal displacements and zero shear stresses were applied throughout the specimen center plane. The FE mesh used (if not indicated otherwise) consists of 85824 8-node linear displacement brick elements with reduced integration (C3D8R, see [5]) and is partly shown in Fig. 16.

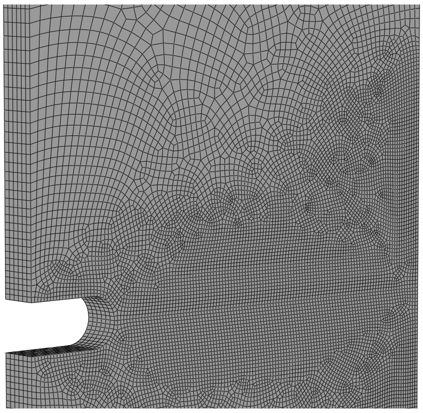

Figure 16: Finite element model of half the SENT specimen exploiting symmetry with respect to center plane.

The three-dimensionality of the stress state throughout the specimen is illustrated in Fig. 17 in terms of the distribution of hydrostatic stress σ_m which attains significantly higher values in the specimen center plane than on the free surface.

5.1 Plastic zone formation at a notch

The zone of intense inelastic deformation that develops at a notch or crack tip prior to and during fracture is generally of great interest as it is directly related to the amount of energy dissipation and hence the fracture toughness of a material. Much work, hence, has been devoted to its numerical analysis in case of neat (e.g. [19],[18]) as well as rubber-toughened thermoplastics (see, e.g., [30] for a review). For instance, addressing in particular PC/ABS blends, their two-phase microstructure has been explicitely resolved in a 2D plane strain model considering a crack tip under mode I small scale yielding conditions in [26]. Since

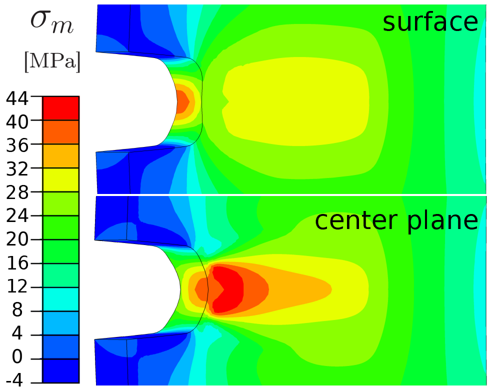

Figure 17: Contours of hydrostatic stress σ_m on SENT specimen surface (top) and in center plane (bottom) at a specimen elongation of $u = 2.5$ mm (prior to fracture) simulated for PC/ABS(70/30) using the Raghava model.

such a micromechanical (”bottom up”) approach significantly suffers from the lack of knowledge about the individual constituent behavior on the blend microscale as well as from idealizations in modeling the microstructure, here a macroscopic (”top down”) approach towards analyzing the plastic zone at a notch is pursued.

In the following, the evolution of the plastic zone ahead of the SENT specimen notch is simulated utilizing the different models discussed above. For both PC/ABS materials, numerical results are compared to the experimental findings in Sect. 2.2. As it has turned out that the plastic zone shapes predicted using the Drucker-Prager and Raghava model are very similar prior to fracture, only results from the Raghava model and the Green/Gurson-like model are shown in the present section. For a direct comparability with the experimental results in Fig. 6 the deformation zones are presented in the following in terms of the total strain in the tensile direction, which corresponds to plastic strain in view of only small elastic strains. Contours of the logarithmic strain in the tensile direction at the specimen center plane and at the free surface computed from the Raghava model are shown for PC/ABS(45/55) in Fig. 18 and for PC/ABS(70/30) in Fig. 19, respectively. The graphs refer to the same two successive loading stages (in terms of overall specimen elongation u) as the experimental data in Fig. 6.

Generally, the elongated shape of the plastic zone (being typical for rubber-toughened thermoplastics, e.g. [30]) appears to be reasonably captured by the simulations for both materials in comparison with the experiments in Fig. 6. Also, its larger extension in case of PC/ABS(45/55) in Fig. 18 compared to PC/ABS(70/30) in Fig. 19 corresponds to the experimental findings (Fig. 6). The view into the notch root (center of Figs. 18 and 19) indicates necking at the specimen surface which was also observed in the experiments.

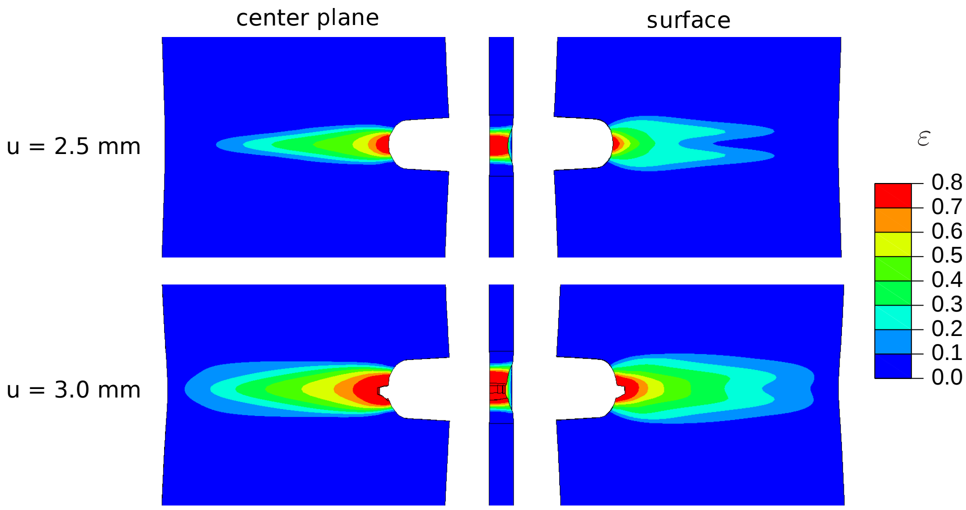

Figure 18: Zone of intense (∼plastic) strain in loading direction at notch in PC/ABS(45/55) simulated using the Raghava model at two successive stages of specimen elongation u.

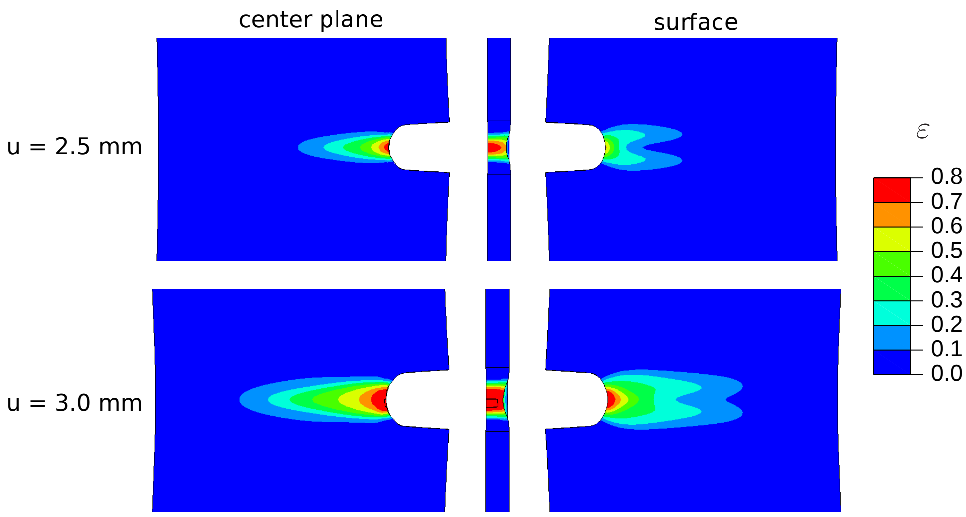

Figure 19: Zone of intense (∼plastic) strain in loading direction at notch in PC/ABS(70/30) simulated using the Raghava model at two successive stages of specimen elongation u.

It should be noted that these findings hold for all experimental tests (with only one per material shown in Fig. 6); this corresponds to the rather small amount of scatter in the experimental load-displacement curves in Fig. 7. For both materials, the simulated deformation zone clearly changes from the interior of the specimen (center plane) to the free surface, which can be attributed to the differences in hydrostatic stress (see Fig. 17) that promotes volumetric plastic flow. In case of PC/ABS(45/55), however, the predicted splitting of the deformation zone at the specimen surface, particularly in the earlier loading stage ($u = 2.5\,\text{mm}$, see Fig. 18 top right), does not agree with experimental observations (Fig. 6a and c). The simulated transition from a single localized deformation zone in the specimen interior to two branches at the free surface indicates plastic flow by a through-thickness-slip mode (well known from plastically incompressible materials under plane stress). In the real PC/ABS(45/55), however, such a deformation pattern appears to be not present (Fig. 6a and c).

Contrarily, in case of PC/ABS(70/30) – the behavior of which is dominated by the larger amount of the plastically incompressible PC – the computed splitting of the deformation zone at the specimen surface (Fig. 19 right) is in fact also visible (though not very clear) in the experiments (Fig. 6b and d). This might indicate that the suitability of dilatant plasticity models of the Raghava (or Drucker-Prager) type to capture the deformation behavior of PC/ABS blends under complex loading states with an elevated stress triaxiality is limited to grades with only a moderate amount of ABS.

Figure 20 shows the deformation zone computed using the Green/Gurson-like model in case of PC/ABS(45/55); pretty similar results (not shown for brevity) are obtained from this material model also for PC/ABS(70/30). These numerical results illustrate

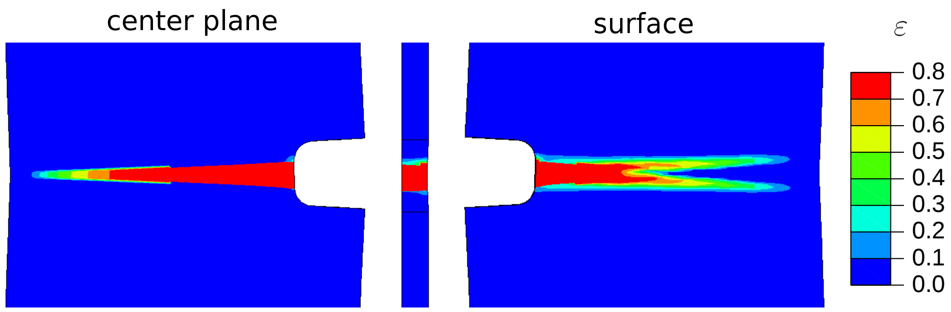

Figure 20: Zone of intense ($\sim$plastic) strain in loading direction at notch in PC/ABS(45/55) simulated using the Green/Gurson-like model at specimen elongation of $u = 2.5\,\text{mm}$.

(analogous to earlier studies, see e.g. [30]) that this type of model which is governed by an evolving porosity, overemphasizes the localization of inelastic deformation and hence predicts unrealistic narrow deformation zones at a notch. This is despite the fact that the calibrated Green/Gurson-like model well captures the response of PC/ABS under uniaxial tension including the progressive hardening at large strains (Fig. 10). Yet, the shady behavior of this model, giving rise to the results in Fig. 20, could already be anticipated from its response under elevated stress triaxialities depicted in Fig. 14. Owing to the large volume strain predicted by the Green/Gurson-like model in such a situation

(Fig. 15), necking at the specimen surface did not occur in the finite element simulation (see Fig. 20, center). Because of its failure to realistically reproduce the deformation zone at a notch, the Green/Gurson-like model is not further considered in the simulation of crack propagation in PC/ABS in Sect. 5.2.

The above observations made by comparing the performance of the Raghava, the Drucker-Prager and the Green/Gurson-like model suggest that an evolving porosity has a much stronger influence on the plastic zone formation at a notch than the shape of the yield surface. This was confirmed by simulations carried out using the Green/Gurson-like model with the evolution of the porosity switched off, which led to plastic zone shapes rather similar to those obtained using the Raghava or the Drucker-Prager model.

The finding within the present study that the Drucker-Prager and the Raghava model – despite their different yield surface shapes – lead to almost identical results, has to be taken with some caution. In case of the considered specimen geometry (with a notch radius comparable to the specimen thickness) and the coarse modeling of crack advance by the elimination of (not very small) finite elements (see Sect. 5.2), the simulated local stress triaxiality ahead of the crack did not exceed a value of 1.5 for which the response of the two models in terms of their yield surface shape (Figs. 8 and 9) is still pretty close. A deviation of the models' responses may, however, be expected for specimens with a significantly sharper notch giving rise to higher local stress triaxialities.

5.2 Simulation of fracture behavior

As a further inspection of the suitability of the different material models to capture the behavior of PC/ABS blends, the fracture tests reported in Fig. 7 are simulated. The Green/Gurson-like model thereby is discarded because of its failure to reproduce the plastic zone already prior to fracture (Fig. 20). While the Raghava and the Drucker-Prager model yield almost identical results in terms of the pre-fracture deformation zone at the SENT specimen notch, it is of interest whether the different shape of their yield loci at elevated stress triaxiality (see Figs. 8 and 9) becomes noticeable in the situation of an advancing crack front being much sharper than the initial notch.

Crack propagation in the present work is modeled numerically in a rather coarse manner by the deletion of finite elements (see Fig. 21) upon fulfillment of a local failure criterion. Two common criteria (among various others available in the literature; see, e.g., [10]) are considered here which state that ductile failure takes place at a critical value of accumulated plastic strain

$$\varepsilon^p = \int_0^t \sqrt{\boldsymbol{D}^p : \boldsymbol{D}^p} dt \geq \varepsilon^p_{crit} \tag{11}$$

or, alternatively, at a critical value of plastic work per unit volume

$$w^p = \int_0^t \boldsymbol{\sigma} : \boldsymbol{D}^p dt \geq w^p_{crit} \quad . \tag{12}$$

Only the failure parameters ε^p_{crit} or w^p_{crit} are calibrated in simulating the fracture tests (Tab. 3) in order to match the onset of crack propagation which coincides with the peak of the load displacement curves shown in Figs. 22 and 23. All other material parameters (governing the deformation behavior) are taken fixed as calibrated from the uniaxial tensile tests (Tab. 1 and 2). It should be mentioned that local failure strains calibrated using (11) or (12), see Tab. 3, are significantly larger that those measured in the uniaxial tensile tests ($\sim 0.6...0.8$) up to which the deformation behavior of the constitutive models has been calibrated in Sect. 4.

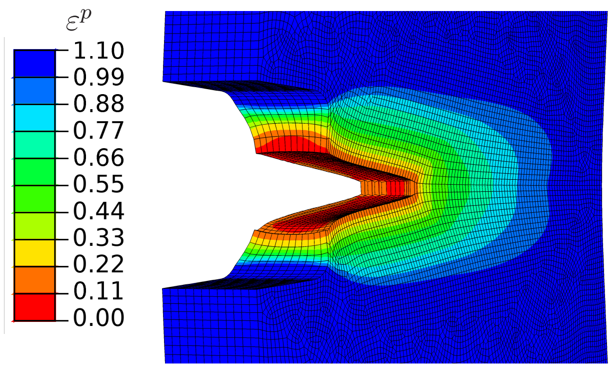

Figure 21: Advancing crack in SENT specimen of PC/ABS(70/30) modeled by deletion of fiite elements, and distribution of accumulated plastic strain computed from Raghava model at specimen elongation of $u = 3.4$ mm.

As depicted in Figs. 22 and 23, both the Raghava and the Drucker-Prager model, once calibrated to the uniaxial tensile test data and endowed with either of the two failure criteria (11) or (12), lead to a reasonable reproduction of the force displacement curves from the SENT fracture experiments for PC/ABS(45/55) as well as PC/ABS(70/30). At closer inspection it is noticeable that the simulation results in case of PC/ABS(45/55), see Fig. 22, are almost independent of the material model and the failure criterion, and they all overestimate the displacement at ultimate specimen failure. In contrast, the simulated force displacement curves for PC/ABS(70/30), see Fig. 23, in the crack propagation regime depart from each other (depending on the material model and failure criterion) and scatter around the experimental data. These observations regarding the simulated specimen response in the crack propagation regime (Figs. 22 and 23) should, however, be taken with caution since the calibrated model responses (see Figs. 10, 11 and 12) increasingly

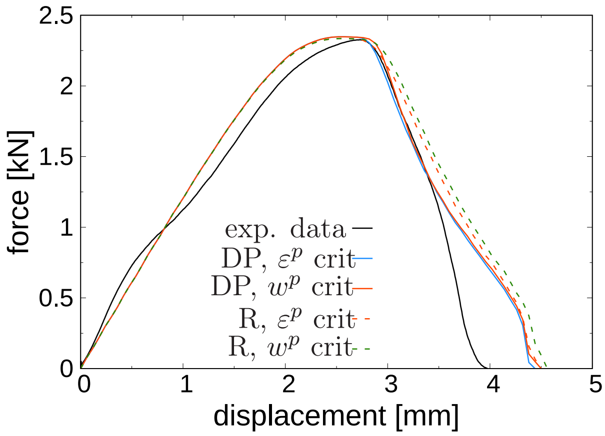

Figure 22: Force displacement curves of SENT fracture tests for PC/ABS(45/55) simulated with different material models and failure criteria in comparison to experimental data (averaged).

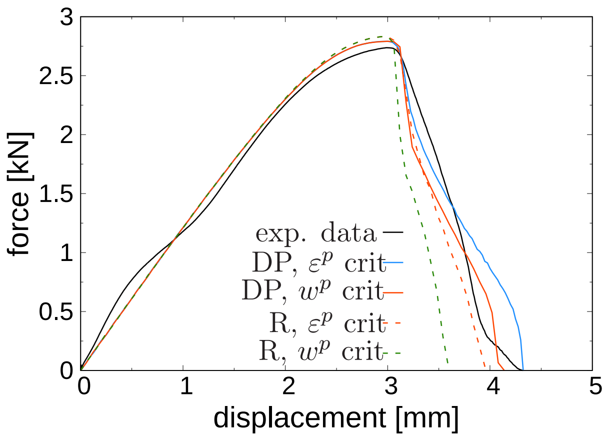

Figure 23: Force displacement curves of SENT fracture tests for PC/ABS(70/30) simulated with different material models and failure criteria in comparison to experimental data (averaged).

depart from each other and from the experimental data for strains beyond 0.7 while much larger local strains occur in the fracture simulations (see Tab. 3). Also, the results might be affected by the coarse numerical modeling of crack advance as discussed below.

Since crack propagation here is modeled simply by eliminating finite elements upon fulfillment of a local failure criterion, the issue of mesh dependence deserves special attention, e.g. [10]. A comparison of the simulated force-displacement curves obtained for three differently fine meshes in Fig. 24 clearly shows that the predicted crack initiation as well as the crack propagation behavior are indeed mesh dependent with a coarser mesh (at fixed value of the failure parameter) leading to a delayed overall specimen failure.

Since only the crack propagation regime suffers from mesh dependence, this effect could be overcome by calibrating the local failure parameters ε^p or w^p_{crit} to the size of the finite elements. What is here referred to as the "fine" mesh is the standard mesh with 85824 elements used throughout this work. The "medium" and the "coarse" mesh consist of 26520 and 14544 finite elements, respectively. The relative minimum element lengths are given in Table 4 in the Appendix.

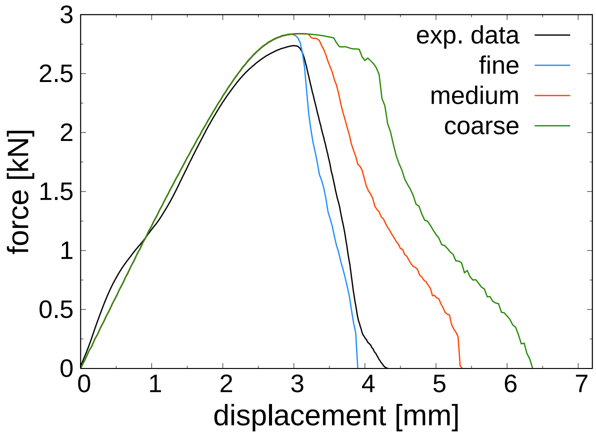

Figure 24: SENT fracture test for PC/ABS(70/30) simulated using the Raghava model with the ε^p_{crit} failure criterion calibrated to the fine mesh.

6 Summary and conclusions

The motivation of this work was twofold: On the one hand side, it presents an experimental investigation of the large strain deformation and fracture behavior of rubber-toughened PC/ABS blends with a focus on the effect of blend composition. In doing so, the local measurement of strain fields through digital image correlation (DIC) enabled the determination of the true stress and volumetric strain response in uniaxial tensile tests as well as the evolution of the plastic zone in notched SENT specimens prior to and during fracture. On the other hand, different material models – all featuring a plastically dilatant behavior under tension – are systematically analyzed with regard to their capability to describe the mechanical response of the considered PC/ABS materials. These models are chosen as simple as possible to be useful for practical applications such as structural finite element analyses of technical components. The focus thereby was not on a perfect fit but rather on the investigation of the effect of basic features such as yield surface shape and porosity evolution.

The experimental results on two commercial PC/ABS blends with fairly different compositions (PC vs. ABS content) show a clear influence of the composition on the deformation and fracture behavior, which is in line with various earlier studies in the literature. The latter, however, are typically less complete in presenting data on the true stress-strain response along with the accompanying evolution of volume strain, which are both needed for an adequate calibration of constitutive models.

The three "classical" isotropic constitutive models investigated here are the Drucker-Prager and the Raghava model, which differ only by the shape of the yield surface, and a Green/Gurson-like model, which additionally displays a dependence of the yield surface on the evolving porosity (representing microscale damage mechanisms). These models all proved to well capture the true stress-strain response as well as the evolution of volume strain of the two PC/ABS blends in uniaxial tensile tests, yet they show a rather ambivalent performance in finite element simulations of the SENT fracture tests.

Key findings and conclusions from this study are itemized in the following.

- The zone of intense (plastic) deformation that develops at a notch or crack tip in the course of loading (including crack propagation) is experimentally found to vary in shape with the blend composition. In particular, in PC/ABS blends with a large amount of the plastically incompressible PC the crack-tip plastic zone exhibits features such as splitting at the specimen surface (likely due to through-thickness-slip) which is reminiscent of plastically incompressible materials. In ABS-rich blends, in contrast, a single highly elongated plastic zone similar to that in neat ABS, e.g. [13], is observed.

- In simulations of the SENT fracture tests on both materials it turned out that (Green/Gurson-like) models which account for an increasing porosity and thus feature a shrinkage of the yield surface under high stress triaxiality (as prevailing at a notch) severly overestimate the localization of plastic strain and hence are not suited to describe the behavior PC/ABS blends. This corresponds to findings from other studies applying such a type of model to rubber-toughened polymers as discussed, e.g., in [30].

- In contrast, plastically dilatant material models which do not feature a shrinkage of the yield surface with plastic volume strain, such as the Drucker-Prager and the Raghava model appear to be quite successful in simulations of the overall response of PC/ABS in SENT fracture tests.

- A closer inspection, however, indicates that the suitability of the simple isotropic models of Drucker-Prager or Raghava type is limited to PC/ABS grades with a relatively small amount of ABS. In case of the ABS-rich material, these models showed larger deficiencies in reproducing the plastic zone shape as well as the fracture behavior (overall force-displacement response). One may hence conclude that the complex behavior of ABS – e.g. its overall anisotropy due to the effect of distributed crazing [13] – needs to be also accounted for in modeling the mechanical behavior of ABS-rich PC/ABS blends.

- Through these findings, the present study provides some indication of the range of applicability of established (i.e. easy to use) material models for numerical structural analyzes of technical components made of PC/ABS – which is of practical value.
- On the other hand, the revealed limitations of the above discussed models indicate needs for further fundamental research on the improved constitutive modeling of PC/ABS, possibly supported by multiscale modeling.

Acknowledgement

Financial support of this work by the German Science Foundation (DFG) under grant no. SE 872/6-1 is gratefully acknowledged. Also, the authors gratefully acknowledge the laboratory assistance by W. Wendler as well as the kind supply of the analyzed materials by Dr. S. Hobeika (Covestro).

References

[1] Belytschko, T., Liu, W. K., Moran, B., and Elkhodary, K. (2013). *Nonlinear finite elements for continua and structures*. Wiley.

[2] Bubeck, R. A., Buckley, D. J., Kramer, E. J., and Brown, H. R. (1991). Modes of deformation in rubber-modified thermoplastics during tensile impact. *J. Mat. Sci.*, 26(23):6249–6259.

[3] Chiang, W.-Y. and Hwung, D.-S. (1987). Properties of polycarbonate/acrylonitrile-butadiene-styrene blends. *Pol. Eng. Sci.*, 27(9):632–639.

[4] Danielsson, M., Parks, D. M., and Boyce, M. C. (2007). Micromechanics, macromechanics and constitutive modeling of the elasto-viscoplastic deformation of rubber-toughened glassy polymers. *J. Mech. Phys. Solids*, 55:533–561.

[5] Dassault Systèmes (2013). *Abaqus Analysis User's Guide, Abaqus 6.13.* Vélizy-Villacoublay.

[6] De Souza Neto, E. A., Peric, D., and Owen, D. R. J. (2011). *Computational methods for plasticity: theory and applications.* Wiley.

[7] Fang, Q.-Z., Wang, T. J., Beom, H. G., and Zhao, H. P. (2009). Rate-dependent large deformation behavior of PC/ABS. *Polymer*, 50(1):296–304.

[8] Greco, R. (1996). Polycarbonate toughening by ABS. *In: Martuscelli, E. et al. (Eds), Advanced Routes for Polymer Toughening.*, pages 469–526.

[9] Green, R. J. (1972). A plasticity theory for porous solids. *Int. J. Mech. Sci.*, 14(4):215–224.

[10] Gross, A. and Ravi-Chandar, K. (2014). Prediction of ductile failure using a local strain-to-failure criterion. *Int. J. Fract.*, 186:69–91.

[11] G'Sell, C., Hiver, J., Dahoun, A., and Souahi, A. (1992). Video-controlled tensile testing of polymers and metals beyond the nacking point. *J. Mat. Sci.*, 27:5031–5039.

[12] Gurson, A. L. (1977). Continuum theory of ductile rupture by void nucleation and growth. *J. Eng. Mat. Technol.*, 99:2–15.

[13] Helbig, M., Van der Giessen, E., Clausen, A. H., and Seelig, T. (2016). Continuum-micromechanical modeling of distributed crazing in rubber-toughened polymers. *Eur. J. Mech. A/Solids*, 57:108–120.

[14] Hiermaier, S. and Huberth, F. (2012). Volume dilation in a polycarbonate blend at varying strain rates. *Eur. Phys. J. Special Topics*, 206:173–181.

[15] Inberg, J. (2001). Fracture of polycarbonate/ABS blends. *PhD thesis, University of Twente.*

[16] Inberg, J. and Gaymans, R. (2002). Co-continuous polycarbonate/ABS blends. *Polymer*, 43:2425–2434.

[17] Ishikawa, M. (1995). Stability of plastic deformation and toughness of polycarbonate blended with poly(acrylonitrile-butadiene-styrene) copolymer. *Polymer*, 36(11):2203–2210.

[18] Kattekola, B., Ranjan, A., and Basu, S. (2013). Three dimensional finite element investigations into the effects of thickness and notch radius on the fracture toughness of polycarbonate. *Int. J. Frac.*, 181:1–12.

[19] Lai, J. and Van der Giessen, E. (1997). A numerical study of crack-tip plasticity in glassy polymers. *Mech. Mater.*, 25:183–197.

[20] LIMESS GmbH (2009). *Digital Image Correlation. Q-400 Operation Manual.* Krefeld.

[21] Lombardo, B. S., Keskkula, H., and Paul, D. R. (1994). Influence of ABS type on morphology and mechanical properties of PC/ABS blends. *J. Appl. Pol. Sci.*, 54(11):1697–1720.

[22] Nigam, I., Nigam, D., and Mathur, G. N. (2005). Effect of rubber content in ABS on properties of PC/ABS blends. *Pol.-Plast. Tech. Eng.*, 44:815–832.

[23] Polanco-Loria, M., Clausen, A. H., Berstad, T., and Hopperstad, O. S. (2010). Constitutive model for thermoplastics with structural applications. *Int. J. Impact Eng.*, 37(12):1207–1219.

[24] Raghava, R., Caddell, R. M., and Yeh, G. S. Y. (1973). The macroscopic yield behaviour of polymers. *J. Mat. Sci.*, 8:225–232.

[25] Seelig, T. and Van der Giessen, E. (2002). Localized plastic deformation in ternary polymer blends. *Int. J. Solids Structures*, 39:3505–3522.

[26] Seelig, T. and Van der Giessen, E. (2007). Effects of microstructure on crack tip fields and fracture toughness in PC/ABS polymer blends. *Int. J. Fract.*, 145:205–222.

[27] Seidler, S. and Grellmann, W. (1993). Fracture behaviour and morphology of PC/ABS blends. *J. Mat. Sci.*, 28(15):4078–4084.

[28] Suarez, H., Barlow, J. W., and Paul, D. R. (1984). Mechanical properties of ABS/polycarbonate blends. *J. Appl. Pol. Sci.*, 29(11):3253–3259.

[29] Tan, Z. Y., Xu, X. F., Sun, S. L., Zhou, C., Ao, Y. H., Zhang, H. X., and Han, Y. (2006). Influence of rubber content in ABS in wide range on the mechanical properties and morphology of PC/ABS blends with different composition. *Pol. Eng. Sci.*, 46(10):1476–1484.

[30] Van der Giessen, E. and Seelig, T. (2015). Computational modeling of rubber-toughening in amorphous thermoplastic polymers: a review. *Int. J. Fract.*, 196(1):207–222.

[31] Wang, H., Zhou, H., Huang, Z., Zhang, Y., Qiao, H., and Yu, Z. (2016). Experimental investigation and modeling of the mechanical behavior of PC/ABS during monotonic and cyclic loading. *Polymer Testing*, 50:216–223.

[32] Wildes, G., Keskkula, H., and Paul, D. R. (1999). Fracture characterization of PC/ABS blends: effect of reactive compatibilization, ABS type and rubber concentration. *Polymer*, 40(25):7089–7107.

A Material parameters of all models for both materials

Table 1: Material parameters calibrated for PC/ABS(45/55)

Parameter	Drucker-Prager	Raghava	Gurson
E [MPa]	1500	1500	1500
ν	0.37	0.37	0.37
$\dot{\varepsilon}_0$ [s^{-1}]	0.01	0.01	0.01
A [MPa^{-1}]	0.65	0.46	0.38
α	0.546	55 MPa	8
β_1 [MPa]	55	55	55
β_2 [MPa]	6	5	6
β_3	31.25	29.41	37.5
β_4 [MPa]	34.94	22.15	85.94
β_5	2.5	2	2
f_0	–	–	0.1

Table 2: Material parameters calibrated for PC/ABS(70/30)

Parameter	Drucker-Prager	Raghava	Gurson
E [MPa]	1500	1500	1500
ν	0.40	0.40	0.40
$\dot{\varepsilon}_0$ [s^{-1}]	0.01	0.01	0.01
A [MPa^{-1}]	0.57	0.4	0.33
α	0.48	57 MPa	8
β_1 [MPa]	65	66	68
β_2 [MPa]	5	5	3
β_3	15	11	3
β_4 [MPa]	60	50	170
β_5	3.0	3.0	2.9
f_0	–	–	0.1

Table 3: Failure parameters calibrated for fine mesh (SENT specimen), see Tab. 4 and Fig. 24

Material	PC/ABS(45/55)		PC/ABS(70/30)	
Model	Drucker-Prager	Raghava	Drucker-Prager	Raghava
w^p_{crit} [MPa]	70	75	77.5	76
ε^p_{crit} [-]	1.13	1.24	1.05	1.07

Table 4: Variation of the FE mesh parameters

FE mesh	fine	medium	coarse
rel. min. el. length	1	2	2.67
no. of elements	85824	26520	14544